

MEASURING THE MAGNETIC FLUX QUANTUM VIA $\text{YBa}_2\text{Cu}_3\text{O}_{7-\delta}$
SUPERCONDUCTING QUANTUM INTERFERENCE DEVICES

by

C. P. Strehlow

A senior thesis submitted to the faculty of

Ithaca College

in partial fulfillment of the requirements for the degree of

Bachelor of Science

Department of Physics

Ithaca College

May 2009

Copyright © 2009 C. P. Strehlow

All Rights Reserved

ITHACA COLLEGE

DEPARTMENT APPROVAL

of a senior thesis submitted by

C. P. Strehlow

This thesis has been reviewed by the research advisor, senior thesis instructor,
and department chair and has been found to be satisfactory.

Date

Dr. M. C. Sullivan, Advisor

Date

Dr. B. G. Thompson, Advisor

Date

His Majesty, Luke Keller, Senior Thesis Instructor

Date

Bruce Thompson, Chair

ABSTRACT

MEASURING THE MAGNETIC FLUX QUANTUM VIA $\text{YBa}_2\text{Cu}_3\text{O}_{7-\delta}$ SUPERCONDUCTING QUANTUM INTERFERENCE DEVICES

C. P. Strehlow

Department of Physics

Bachelor of Science

Superconducting thin films of Yttrium Barium Copper Oxide ($\text{YBa}_2\text{Cu}_3\text{O}_{7-\delta}$) were grown and photolithographic techniques were used to pattern the films into Superconducting QUantum Interference Devices (SQUIDs). We wired the SQUIDs and attempted to measure the magnetic flux quantum. Unfortunately, the samples lost oxygen content during processing, causing degradation of and in some areas complete loss of the superconducting phase. The expectation of oxygen degradation occurring during processing was confirmed by the measurement of the final remaining unprocessed bi-crystal sample, which was wired and measured with no processing, and showed a transition temperature of 80K. Possible causes are discussed as well as methods for avoiding oxygen loss in future processing.

ACKNOWLEDGMENTS

In chronological order of this project's progression, the author would like to thank all those who assisted in its completion. First, from the Center for Nanophysics and Advanced Materials, Dr. Richard Green's Pulsed Laser Deposition Lab and Research Group, and second, The Faculty and Staff of the Cornell Nanoscale Science and Technology Facility. Thanks to the Physics Department at Ithaca College, The Provost of Ithaca College, the Educational Grant Initiative, and NSF Grant DMR 0607557 for all financial support. Thanks to Ron Gilmore, Ithaca College Science Librarian for help with research.

Contents

Table of Contents	vii
List of Figures	ix
1 Introduction	1
1.1 A Brief History of Superconductivity	1
1.2 Superconducting QUantum Interference Devices	2
2 Experimental Apparatus	5
2.1 YBCO Samples	6
2.2 Wiring and Measurement	7
2.2.1 Chrome and Gold Contact Evaporation	7
2.2.2 Wiring	8
2.3 Dewar/Vacuum Chambers	10
2.3.1 Vacuum Feedthroughs	10
2.3.2 μ -metal and IR shielding	12
2.3.3 8-pin Amphenol to Tri-Ax conversion Boxes	15
2.3.4 Tri-ax wires	16
2.4 Instruments	17
3 Theory	19
3.1 R vs. T theory	20
3.2 Josephson Junction Theory	21
3.2.1 Coupled Wavefunctions and Weak Linking	21
3.2.2 DC Josephson Effect	24
3.2.3 AC Josephson Effect	26
3.3 SQUID Theory	27
4 Data Presentation and Analysis	31
4.1 Resistance vs. Temperature Measurements	31
4.2 Analysis of Data	37
5 Conclusion	41

A Pulsed Laser Deposition	45
A.1 Sample Cleaning	45
A.2 Chamber Cleaning and Sample mounting	46
A.3 Initial pump down and Pre-ablation	46
A.4 Second pump down	47
A.5 Deposition	47
A.6 Annealing	47
A.7 AC Susceptibility	48
B Photolithography	49
B.1 Layout Editor	50
B.2 Mask Making	51
B.3 Primary Photoresist Spinning	52
B.4 Primary Photoresist Exposure and Development	52
B.5 Phosphoric Acid Etching	53
B.6 Ion Milling	53
B.7 Secondary Photoresist Spinning, Exposure and Development	54
C Layout Editor	57
D Experimental Apparatus Photos	63
Bibliography	67

List of Figures

2.1	photo of fully wired BCJ2 horizontal	8
2.2	photo of fully wired BCJ2 vertical	9
2.3	Picture of the Dewar/Vaccum Chamber	11
2.4	Vacuum Feedthroughs	12
2.5	IRshield1	13
2.6	IRshield2	14
2.7	Conversion Boxes	15
2.8	Tri-Ax Wires	16
2.9	CNS 211 Experimental Setup	17
3.1	Theory diagram 1	23
3.2	Theory diagram 2	24
3.3	Theory diagram 3	28
4.1	Resistance vs Temperature plots for SQUIDs on BCJ3	32
4.2	Close up of Transition in the Resistance vs Temperature plots for SQUIDs on BCJ3	33
4.3	Resistance vs Temperature plots for SQUIDs on BCJ3 after re-annealing	35
4.4	Resistance vs Temperature plot for un-patterned BCJ1	36
4.5	Phases of YBCO represented as temperature vs. oxygen doping . . .	38
4.6	Resistivity vs. Temperature for selected oxygen dopings in YBCO . .	39
B.1	Image of Final Photolithography Mask	51
B.2	photolithography pattern	53
B.3	Ion Mill Diagram	54
C.1	SQUID 2 microns	59
C.2	4 Element photolithography pattern	59
C.3	Image of Photolithography Mask	60
C.4	photolithography pattern	61
C.5	Josephson Junction 2 microns	61
C.6	RvsT 80 microns	62
C.7	3 Element photolithography pattern	62

D.1	Top of the Dewar/Vaccum Chamber	64
D.2	Picture of the bottom of the Dewar/Vaccum Chamber	65
D.3	Sample Stage	66

Chapter 1

Introduction

For undergraduates quantum mechanics can be daunting and elusive. The subject matter presses the limits of classical logic, knowledge, and intuition. Moreover, without proper instruments to facilitate the experimental proof, such as the human eye, stopwatch, and meter stick may be used to confirm classical mechanics; quantum mechanics is presented to undergraduates in a purely theoretical framework, with little or no hands-on experimental validation provided. In collaboration with my research advisor I decided to provide a medium for that experimental validation for future undergraduate physicists of Ithaca College, by preparing and testing an experimental apparatus which gives students the ability to directly measure quantum mechanical phenomena.

1.1 A Brief History of Superconductivity

Superconductivity was first observed in 1911 by Kamerlingh-Onnes [1] in a sample of high-purity mercury, following his successful liquification of Helium in 1908. Since those early days of low-temperature experiment, superconductivity has been discov-

ered in many different materials. In the decades following the liquefaction of helium, most of the type I superconductors were discovered, including aluminum, tin, and lead. [1] In 1986, Müller and Bednorz discovered a new family of ceramic compounds now known as Cuprate-Perovskite compounds [9]. Cuprate-Perovskite compounds refer to any compound containing Copper Oxide (CuO_2), as well as adhering to a specific structure in the crystal lattice, matching that of the chemical CaTiO_3 , also named perovskite. These new "High Temperature Superconductors" exhibited extremely high critical parameters, including critical temperatures in excess of 100 K and critical magnetic fields in excess of one hundred tesla. In addition to the cost reduction associated with liquid nitrogen cooling, these novel ceramics provided a robust and versatile medium for studying the macroscopic quantum properties of the superconducting wavefunction.

1.2 Superconducting QUantum Interference Devices

The idea of electron tunneling occurring between two superconducting materials across an insulating barrier was first proposed by B.D. Josephson in 1962 [3]. The existence of this Josephson Effect was first observed experimentally in 1963 by Anderson *et al.* [6]. The original experimental apparatus used by Anderson to measure the Josephson effect used two layers of superconducting thin film separated by an insulating oxide layer. Soon after the experimental validation of the Josephson Effect, in 1964, Jaklevic *et al.* [4] proposed the possibility of using the Josephson effect to conduct quantum interference experiments, diffraction experiments, and make high-precision magnetic measurements. The proposed experimental procedure was confirmed a year later, by the same authors [5]. Using multiple sets of linked Josephson

Junctions, Jaklevic *et al.* were able to demonstrate the interference and diffraction of the superconducting electrons' waveforms as they tunneled through the barrier, as well as provide a very accurate measurement of the magnetic flux quantum, $\Phi_0 = \frac{h}{2e}$. Upon the discovery of the Cuprate-Perovskite compounds in 1986, new methods for formulating these so called Superconducting QUantum Interference Devices (SQUIDS) were pioneered. In 1989 Koch *et al.* produced DC SQUIDS based on the weak link property of randomly oriented grain boundaries [7]. Although revolutionary compared to their three layer predecessors, these SQUIDS were crude and critical parameters such as junction width and location were uncontrolled. In 1990 Gross *et al.* produced a $\text{YBa}_2\text{Cu}_3\text{O}_{7-\delta}$ SQUID grown on a SrTiO_3 bicrystal substrate [8], which exhibited high precision and extremely low noise. In the last two decades, numerous applications of these low-noise high- T_c SQUIDS have been discovered, including: High precision magnetometers, magnetoencephalographs, magneto resonance imaging machines, scanning microscopy, high frequency radio receivers, and even as a component on the gyroscope of NASA's Gravity Probe B [12]. Due to this low noise characteristic and the high precision resulting from the controlled growth, it was this method of SQUID fabrication that I chose to incorporate into my thesis work.

Chapter 2

Experimental Apparatus

This entire project is centered around 18 superconducting thin films of $\text{YBa}_2\text{Cu}_3\text{O}_{7-\delta}$ which I grew this past summer using pulsed laser deposition at the Center for Nanophysics and Advanced Materials at The University of Maryland at College Park. For details and more information on pulsed laser deposition, refer to Appendix A. The samples were then processed and patterned at the Cornell Nanoscale Science and Technology Facility at Cornell University. For more information on Photolithography, refer to Appendix B. For more information on the pattern design process, refer to Appendix C. All measurements of these samples have been conducted in the Center for Natural Sciences at Ithaca College, either in a helium/nitrogen dewar or the low-temperature lab closed cycle cryogenic cooling system. Each cryogenic chamber passes connections through hermetically sealed feedthroughs to nanovoltmeters and current sources, which have been programmed for data acquisition using LabView.

2.1 YBCO Samples

Studying the properties of the superconducting wavefunction requires high precision measurements and a controlled environment. In order to have a controlled environment, the crystalline lattice of the superconducting material must be uniform and continuous throughout. To attain this kind of control over crystal growth, substrates are chosen with lattice parameters identical to those of the crystal to be grown. In the case of $\text{YBa}_2\text{Cu}_3\text{O}_{7-\delta}$, and all other Pervoskite lattice type crystals, SrTiO_3 provides an almost perfect match in lattice vectors. This allows for uniform crystal growth, and – in best case scenarios – samples that display the ideal superconducting properties of the material. None of the samples I prepared during summer 2008 were ideal, although some were within one Kelvin of the maximum critical temperature, (T_c), in this material, 91K. In total, 13 $5 \times 5\text{mm}^2$ samples were grown, two $10 \times 5\text{mm}^2$ samples were grown, and three $10 \times 5\text{mm}^2$ bi-crystal junction samples were grown; the latter group being the only films capable of producing the Josephson Effect. This is due to the bi-crystal nature of the SrTiO_3 substrates used for these three films. The term bi-crystal means that the substrate is comprised of two separate crystals, only differing from one another in lattice orientation. The bi-crystal substrates we used had one lattice discontinuity line running directly down the middle, with each crystalline lattice rotated 18.5° away from that line in the azimuthal direction, creating a 37° angle between the two lattices. This particular orientation of the SrTiO_3 forces the $\text{YBa}_2\text{Cu}_3\text{O}_{7-\delta}$ to grow in the same bi-crystal junction pattern. This lattice discontinuity produces little or no impedance when in the normal conducting phase, but because of the dependence of the superconducting phase on the lattice, the bi-crystal junction does produce a barrier separating the superconducting wavefunction into two coupled wavefunctions.

2.2 Wiring and Measurement

After the sample processing is complete at the Cornell Nanoscale facility, the samples are returned to Ithaca College and wired for measurement. The sample is mounted on a second substrate, multiple sets of intermediary wires are used to reduce stress on the sample, and all connections are soldered using $Ag - In$ solder.

2.2.1 Chrome and Gold Contact Evaporation

In order to insure a good connection to the sample, an evaporation process is used to layer chrome and gold onto the exposed contacts of the sample. Chrome is used first because it adheres well, and will not lose that property under variations of temperature or pressure. Moreover, gold does not adhere well to $YBa_2Cu_3O_{7-\delta}$, and would be extremely difficult to evaporate onto the sample without chrome. The gold is then used as a second layer for two reasons; one, it is a good electrical conductor, two, covering the chrome with something prevents it from oxidizing, which would make it into an insulator. Once the sample has been coated with chrome and gold, it can be taken out of the evaporation chamber and placed in an acetone bath in the sonicator to be cleaned with high frequency sonic vibrations for five to ten minutes. This removes the contact evaporation pattern of photoresist, exposing the elements and wires of the sample, but leaving all the contact pads coated in the two metals.

Upon measuring the first of the three bi-crystal substrates to be completely processed, we discovered it had de-oxidized out of the superconducting regime, probably to a composition closer to $YBa_2Cu_3O_5$. Many factors may have contributed to this change, however, temperature measurements near the sample stage of the evaporation chamber have been taken in excess of $200^\circ C$, suggesting that the evaporation process may contribute substantially to the degradation of sample composition. Because the

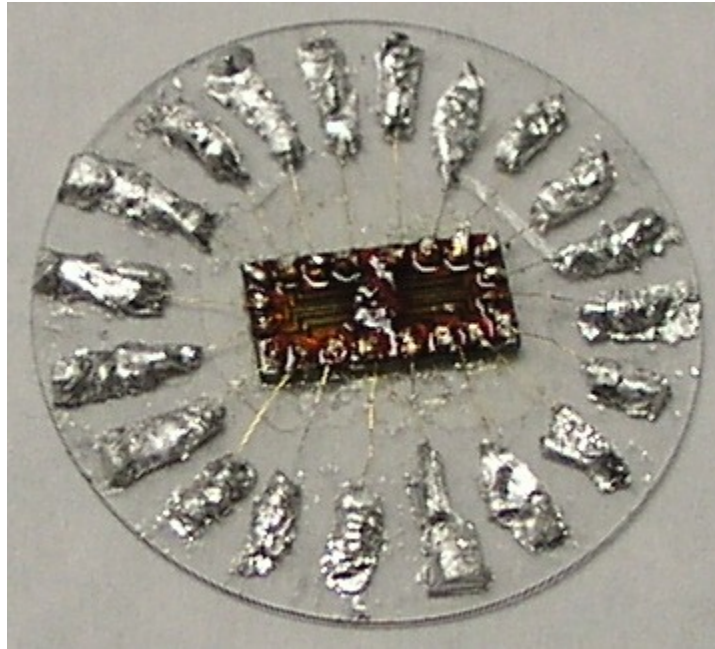


Figure 2.1 Horizontal picture of BCJ 2 fully processed and mounted on sapphire with all connections wired.

first of the three samples was accidentally dropped by a group member, the loss of this second sample meant that every precaution had to be taken to ensure the third sample was processed and wired while preserving its superconducting properties. One step that was eliminated was chrome and gold evaporation. Contact soldering was done very slowly and very carefully using $Ag - In$ solder only.

2.2.2 Wiring

Due to the number of contacts and the dimensions of the sample, a one-inch diameter disc of sapphire was used as a substrate for the sample (see Fig.2.1). Sapphire is used regularly to mount samples for measurement due to its high thermal conductivity and low electrical conductivity. In our case the sapphire mount is larger than normal to accommodate all twenty contacts.

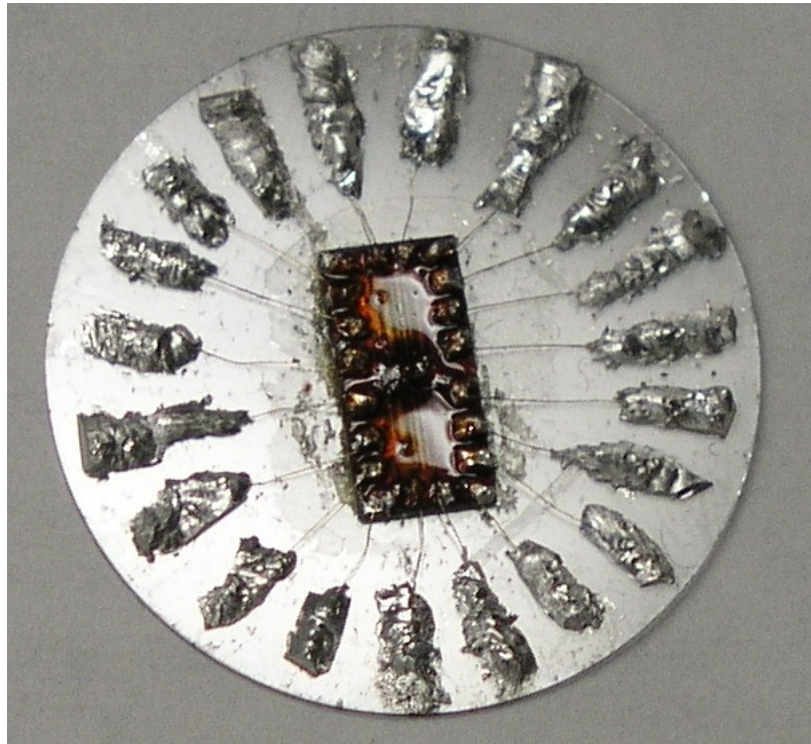


Figure 2.2 Vertical picture of BCJ 2 fully processed and mounted on sapphire with all connections wired.

The sample is mounted in the center of the sapphire, with twenty deposits of *Ag – In* solder spaced 18° apart around the circular mount (see Fig.2.2). These contacts act as a buffer to keep any stresses or strains related to motion of the four-pin wires from affecting the electrical connections to the sample itself. The twenty *Ag–In* deposits are connected to their corresponding $\text{YBa}_2\text{Cu}_3\text{O}_{7-\delta}$ contacts with thin gold wire, used for its ductility and high electrical conductivity. The twenty deposits of indium-silver are then wired to five four-pin connectors, grouped by element, with one four-pin connector for each Josephson Junction, SQUID, and one carrying both positive and negative leads for the magnetic field wires which accompany each SQUID.

2.3 Dewar/Vacuum Chambers

Some of the measurements of these samples have been conducted in a helium/nitrogen dewar maintained with a mechanical roughing pump and a rotary valve turbo pump for sub-Torr pressures. The digital pressure gauge attached to these pumps is dysfunctional, and will only read pressures down to 10^{-4} Torr. In preparation for these measurements, many components of the dewar were repaired or re-fabricated.

2.3.1 Vacuum Feedthroughs

The electrical feedthroughs attached to the dewar were quite old. In addition, there were not enough wires per feedthrough, and the feedthroughs had lost hermetic sealing and would not hold vacuum. Eight-pin hermetically sealed feedthroughs were designed and fabricated in the Ithaca College Physics Department Machine Shop using 1.5" brass rod, Amphenol size 12 eight-pin box mounting hermetically sealed connections and pure indium wire for sealing loose joints. Each feedthrough is wired on the vacuum side to two four-pin female connections, which were passed through



Figure 2.3 Picture of the Dewar / Vacuum Chamber used at IC for some measurements



Figure 2.4 Picture of one of the Vacuum feedthroughs fabricated to fit onto the Dewar in CNS 211

the vacuum chamber and down to the sample stage. On the sample stage, the sample is wired to five separate four-pin connectors, and combinations of three of the five sample four-pins may be wired up at a time to run measurements.

2.3.2 μ -metal and IR shielding

To mitigate the effects of the varying magnetic field's and infrared (IR) radiative heating on the measurement, the sample is completely enclosed in a μ -metal surface and a copper canister. The copper canister was already a component of the dewar when the project began; the μ -metal was cut to size and used to line the inside of the canister to avoid use of any adhesives, while still completely surrounding the sample.



Figure 2.5 Picture of the outer IR shield attached to the bottom of the dewar

Without the μ -metal, all data collected from the SQUIDs would have an uncertainty associated with any changing magnetic fields in the area, including those produced by cellphones, computers, and even the instruments used for the measurement. Without the IR shielding, the outermost canister of the dewar, which is exposed to atmospheric temperatures and pressures, could potentially heat the sample with via IR blackbody radiation. The copper canister also provides shielding form RF radiation, reducing interference with the sample measurements.



Figure 2.6 Picture of both IR shields outside of the dewar

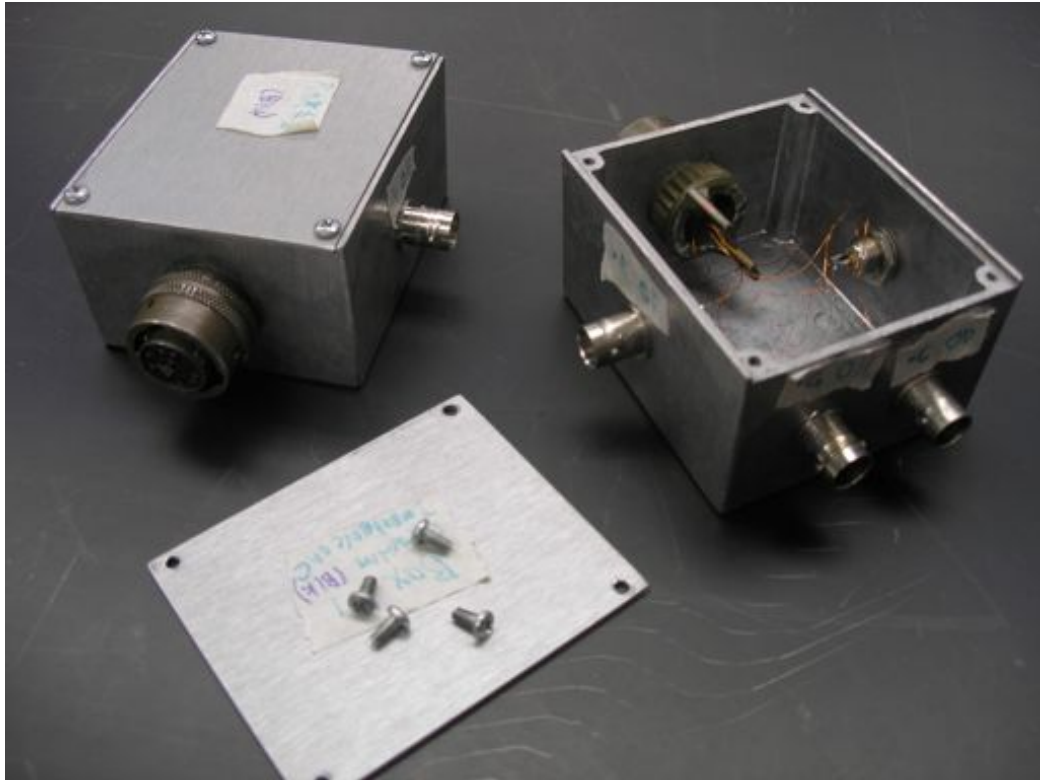


Figure 2.7 Picture of the conversion boxes made for the dewar in 211.

2.3.3 8-pin Amphenol to Tri-Ax conversion Boxes

On the outside of the Dewar, the feedthroughs connect to conversion boxes which were specially fabricated for the project to allow the current sources and nanovoltmeters to interact with the sample while under vacuum. The conversion boxes are $6.6 \times 7.5 \times 4$ cm, and connect to the size 12 8-pin Amphenol box mounting connectors with the corresponding size 12 8-socket box mounting connectors. Within the boxes, the sockets are wired with twisted pair to four separate two-lug tri-ax female box mounting connections.



Figure 2.8 Picture of some of the Tri-Ax wires that were made for this project

2.3.4 Tri-ax wires

Four specialty tri-ax wires were also made for this measurement. Tri-ax was chosen rather than standard BNC because of the extra noise shielding provided by the outer sheath. Two wires connecting tri-ax to tri-ax were made for connecting the current sources to the conversion boxes. Two wires connecting tri-ax to Amphenol millivolt plugs were made for connecting the nanovoltmeter to the conversion boxes. All tri-ax connections used were two-lug, in keeping with the advanced lab standard.



Figure 2.9 Picture of the entire experimental apparatus set up in CNS 211

2.4 Instruments

Instruments used for this measurement include two Keithly 181 nanvoltmeters, two Keithly 224 current sources and one Lakeshore 471 diode thermometer.

Chapter 3

Theory

Since the discovery of superconductivity in 1911, multiple theories have been proposed to describe the two distinct characteristics of the superconducting state. The first is zero resistivity below T_c . In 1933, Walther Meissner and Robert Ochsenfeld discovered the second hallmark property of superconductivity, perfect diamagnetism. The property of perfect diamagnetism was first explained by the British brothers F. and H. London in 1935, who postulated a set of equations that described the magnetic and electric fields within the superconductor. [1] Fifteen years later Ginzburg and Landau expanded on the London equations, producing a theory of superconductivity, now called GL Theory, which was phenomenological in nature, using one wavefunction to describe the superconducting electrons. [1] Seven years later, the first quantitative explanation of the resistivity behavior was proposed by a research group from the University of Illinois at Urbana-Champaign. Dr. John Bardeen and his grad students Leon Cooper and John Schrieffer published the so-called BCS theory, which explained superconductivity through the pairing of electrons within the material via electron-phonon interaction. [1]

To restate that explanation in a classical approximation, one electron attracts

positive nucleus from the immediately adjacent lattice, which creates a net positive charge in the region of that electron. This excess positive charge in turn attracts a passerby electron, effectively pairing the two electrons together into a bosonic particle known as a "Cooper pair". One quality of this new particle is that its two constituent particles have half integer spin, meaning the Cooper Pair has an integer spin and is not subject to the Pauli exclusion principal. This allows for many Cooper pairs to occupy the same quantum state, and in turn the same ground state, bringing the resistance down to zero. One consequence of this shared ground state is that, for continuous single phase superconductors, the wavefunction used to describe a Cooper pair at any point in the lattice is always the same, agreeing quite well with the phenomenological model of the GL Theory. The reason for the temperature dependance of this quantum state is that the electron-phonon interaction that allows for the formation of Cooper pairs is extremely weak and lattice dependent, and is destroyed by thermal agitations present in the material above T_c .

3.1 R vs. T theory

The theory of measuring the resistivity of a superconductor vs. temperature is quite simple. Current is driven through the sample's current leads and the voltage is measured across the voltage leads. Sample voltage data is collected along side thermometer voltage data and when the thermometer voltage corresponds to T_c , an extremely sharp drop in the sample voltage occurs. We know:

$$V = IR \tag{3.1}$$

and, if V has gone to zero, and a known current is still being driven, R must go to zero, or, in other words, the current is being carried by charge carriers in a state

of zero resistance. However, this state of zero resistance is usually overshadowed by contact potentials. Contact potentials occur when two dissimilar conductors or semiconductors are connected, and their Fermi levels do not match. This difference in Fermi levels produces a potential that is independent of applied current, and dependent on absolute temperature. In the case of this measurement, with so many contact interchanges between the instruments and the sample, contact potential offset was large. To screen out these contact potentials, the resistance of the sample is measured using a reverse polarity measurement. This is done by reversing the direction of the current while holding magnitude constant, and measuring the voltage both directions. Taking the difference of the two and dividing by two eliminates the contribution of contact potentials, yielding the true voltage across the sample.

3.2 Josephson Junction Theory

The idea of predictable and measurable quantum mechanical tunneling between two superconductors separated by an insulating barrier was pioneered by B.D. Josephson [3] in 1962, and was derived through the use of a BCS-like wavefunction and quantum mechanical operators. For this reason, the explicit derivation of the AC & DC Josephson and SQUID effects is far too complicated to cover in this paper. To circumvent this minor complication, a phenomenological explanation of the origins of the Josephson Effects will be given using a few basic tenants of superconductivity outlined in the introduction and the beginning of this chapter.

3.2.1 Coupled Wavefunctions and Weak Linking

Consider a superconductor described by an everywhere single-valued wavefunction of the form,

$$\psi(\vec{r}) = \psi_0 e^{i(\vec{q} \cdot \vec{r})} = |\psi(\vec{r})| e^{i\theta(\vec{r})} \quad (3.2)$$

where \vec{q} is the wavevector, \vec{r} is position relative to a chosen origin, and θ is the phase of the wavefunction. Using this wavefunction, a form for the current density subject to an external magnetic field, \vec{A} , can be calculated [2]:

$$j(\vec{r}) = \frac{i\hbar e}{2m} (\psi^* \vec{\nabla} \psi - \psi \vec{\nabla} \psi^*) - \frac{2e^2}{m} (\psi^* \psi \vec{A}). \quad (3.3)$$

Inserting Eqn.3.2 into Eqn.3.3 produces the functional form of the current density which is most convenient for this derivation

$$j(\vec{r}) = \frac{-e}{m} |\psi(\vec{r})|^2 (\hbar \vec{\nabla} \theta(\vec{r}) + 2e \vec{A}). \quad (3.4)$$

Now, assuming this superconductor is in the Meissner state, $j(\vec{r})$ can be assumed to be zero, and

$$\hbar \vec{\nabla} \theta = -2e \vec{A}. \quad (3.5)$$

Integrating this equation around a closed loop, path C, yields

$$\hbar \oint_C \nabla \theta \cdot d\vec{l} = \hbar \Delta \theta = -2e \oint_C \vec{A} \cdot d\vec{l} \quad (3.6)$$

and, given that we are assuming a Ginzburg form of the superconducting wavefunction, the single valued nature implies that any integral around a closed path must constitute a $\Delta \theta$ of $\pm 2\pi n$. Applying Stokes's Theorem to Eqn. 3.6,

$$\Phi = \pm \frac{2\pi n \hbar}{2e} = \pm \frac{n\hbar}{2e} = \pm n \Phi_0 \quad (3.7)$$

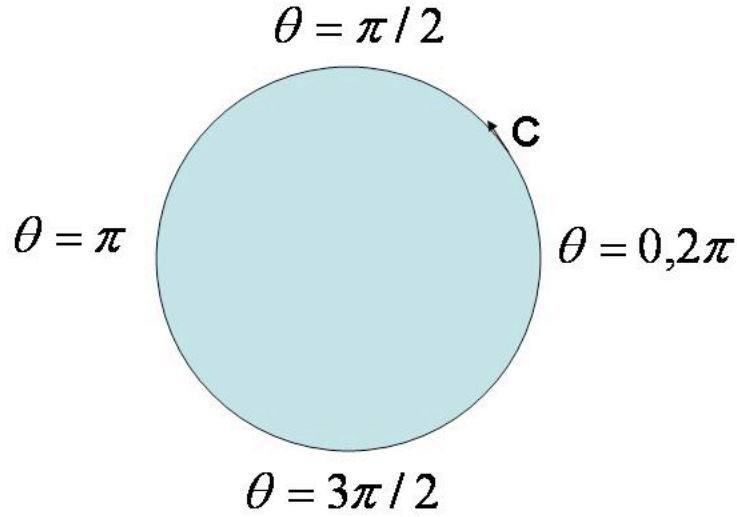


Figure 3.1 closed loop of integration for a superconductor in the Meissner state.

proving that the flux contained in any closed loop within a superconductor is quantized in values of Φ_0 . Also note in Eqn.3.5 the dependence of $\Delta\theta$ on the external magnetic field, \vec{A} .

Consider now the case of two superconducting wavefunctions being separated by an insulating barrier. The wavefunction of the superconductor remains unchanged on either side of the barrier, but, within the barrier, the superconducting wavefunction from each side decays exponentially following a form

$$\psi = e^{i\theta} e^{-K(x+d/2)} \quad (3.8)$$

where θ is the phase of the wavefunction, d is the width of the insulating barrier, K is the penetration depth of the wavefunction into the insulating region, and x is the dimension perpendicular to the barrier. Continuing with the form of Eqn. 3.2 to describe both superconductors, there is now a mixed wavefunction existing in the insulating region, described by the combination of both wavefunctions underneath their respective envelopes of exponential decay.

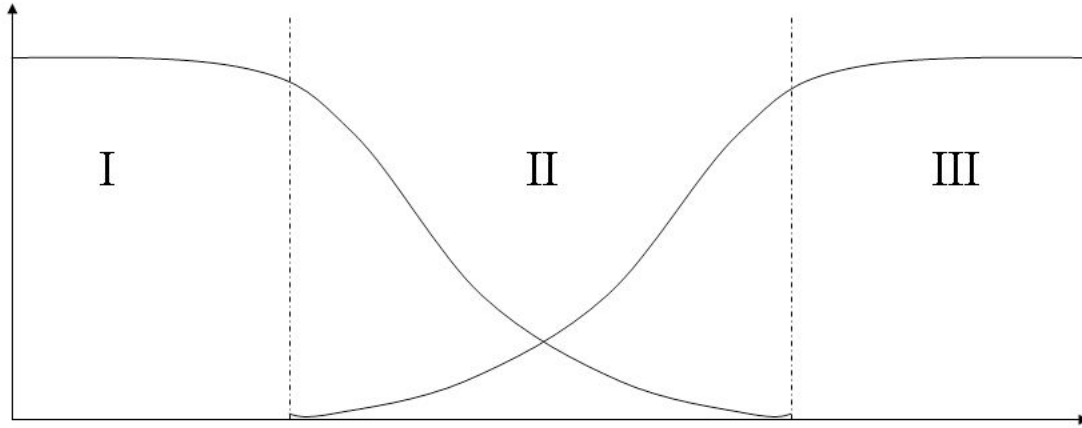


Figure 3.2 Diagram showing the different regions surrounding the bi-crystal junction. In region I, $\psi = e^{i\theta_1}$, in region II, the insulating region, both wavefunctions are considered in a superposition of the form of Eqn. 3.9 and in region III, $\psi = e^{i\theta_2}$

$$\psi = \left(\frac{n_s}{2}\right)^{1/2} (e^{(i\theta_1)K(x+d/2)} + e^{(i\theta_2)K(x-d/2)}) \quad (3.9)$$

with $n_s/2$ being the Cooper pair density. Adhering to our starting assumption of a single valued wavefunction, and assuming no exterior influences (such as applied voltage or driven current), the phases of the two wavefunctions must be equal and the two wavefunctions are said to be coupled. When this coupling exists across a narrow bridge, lattice discontinuity, or even a physical break in the crystal, it is described as a weak link, and is at the heart of the AC & DC Josephson and SQUID effects.

3.2.2 DC Josephson Effect

Now that we have established the nature of the weak linking that produces these macroscopic quantum mechanical effects, we can solve for the functional forms they should exhibit. For the DC Josephson effect, a small current must be driven through

the junction with no applied magnetic field. Inserting Eqn. 3.8 in Eqn. 3.3 and setting the vector potential to zero,

$$j = \frac{ie\hbar n_s}{2m} K e^{-Kd} (-e^{i(\theta_1 - \theta_2)} + e^{i(\theta_2 - \theta_1)}) = j_0 \sin(\delta) \quad (3.10)$$

where

$$\delta = \theta_1 - \theta_2 \quad (3.11)$$

and

$$j_0 = \frac{e\hbar n_s K}{m} e^{-Kd}. \quad (3.12)$$

Driving a current, $j(\vec{r})$, through a Josephson Junction affects the phases of each superconductor, i.e. δ . If the magnitude of the driven current is less than the critical current, j_0 , then the phase difference between the two superconducting wavefunctions on either side of the boundary, δ , adjusts to satisfy Eqn.3.10, which is known as the Josephson Equation. Applied magnetic field would decrease the value of the critical current, j_0 , and attenuate the effect. The current is carried through the Junction via tunneling Cooper pairs, and up to a critical current j_0 the current passes through a potential difference of zero. For driven currents in excess of the critical current j_0 , the superconductivity on either side of the barrier is maintained, but the single value of the crossover region is not, and no Cooper pair tunneling occurs. In this case the current is carried across the barrier by quasi-particles, or un-paired electrons, and produces a non-zero voltage.

3.2.3 AC Josephson Effect

To derive the functionality of the AC Josephson Effect, consider the effect of a finite voltage placed across the junction. Assuming that the applied voltage produces a time dependence in each superconductor's phase,

$$\Psi \propto e^{i\theta(t)} \quad (3.13)$$

and because $\frac{-d\vec{A}}{dt} \cdot d\vec{l} = V$, using Eqn. 3.5 we find,

$$\hbar\left(\frac{\partial\theta_1}{\partial t} - \frac{\partial\theta_2}{\partial t}\right) = 2eV. \quad (3.14)$$

substituting in δ for the θ values,

$$\hbar\frac{\partial\delta}{\partial t} = 2eV. \quad (3.15)$$

assuming a constant voltage, Eqn. 3.15 can be integrated to obtain a value for delta

$$\delta = \frac{2eV}{\hbar}t + \delta_0, \quad (3.16)$$

showing linear behavior in the phase difference between the two superconductors.

Plugging this linear phase form into Eqn. 3.10,

$$j(t) = j_0 \sin\left(\frac{2eV}{\hbar}t + \delta_0\right) \quad (3.17)$$

showing that a finite potential difference across the Junction will produce an AC supercurrent, oscillating at a frequency equal to

$$\nu = \omega/2\pi = 2eV/h = \frac{V}{\Phi_0}. \quad (3.18)$$

Notice again, Φ_0 appears, this time as the ratio of the frequency to the voltage. This behavior is known as the AC Josephson Effect. An applied voltage of one micro-volt produces frequencies on the order of 500 MHz.

3.3 SQUID Theory

Analyzing the above outlined Josephson Effects for the case of two Josephson Junctions connected in a loop with a constant current running through them in parallel can be analogized to the classic interference experiment of shooting photons through two narrow and closely spaced slits. For this reason, this configuration of Josephson Junctions has come to be known under the moniker of the Superconducting Quantum Interference Device. Adapting Eqn. 3.10 to the case of two junctions and applying a trigonometric identity yields

$$j = j_0 \sin(\delta_a) + j_0 \sin(\delta_b) = 2j_0 \cos\left(\frac{\delta_a - \delta_b}{2}\right) \sin\left(\frac{\delta_a + \delta_b}{2}\right) \quad (3.19)$$

with δ_a and δ_b representing the phase differences across each junction respectively. Now, to prove the difference between δ_a and δ_b is quantized by Φ_0 , begin with the functional description of a closed superconducting loop give in Eqn. 3.6

$$\delta_a = \frac{2e}{\hbar} \int_{C_1} \vec{A} \cdot d\vec{l}, \quad (3.20)$$

And

$$\delta_b = \frac{2e}{\hbar} \int_{C_2} \vec{A} \cdot d\vec{l}. \quad (3.21)$$

Adding together Eqn.'s 3.20 & 3.21 obtains a flux dependent form of the cosine argument in Eqn. 3.19

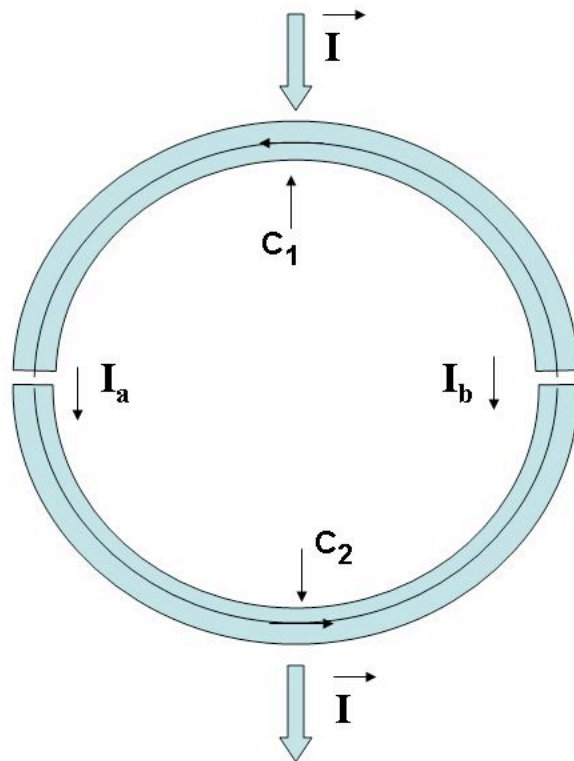


Figure 3.3 Diagram of how a SQUID works, paths of integration, C_1 and C_2 are both labeled, as well as the current leads and instantaneous current across each Josephson Junction

$$\delta_a - \delta_b = \frac{2e}{\hbar} \oint_C \vec{A} \cdot d\vec{l} = \frac{2e\Phi}{\hbar} \quad (3.22)$$

plugging this expression in to Eqn. 3.19 gives a final form for the flux dependent current behavior of a superconducting quantum interference device.

$$j = 2j_0 \cos\left(\frac{e}{\hbar}\Phi\right) \sin\left(\frac{\delta_a + \delta_b}{2}\right) = 2j_0 \cos\left(\pi\frac{\Phi}{\Phi_0}\right) \sin\left(\frac{\delta_a + \delta_b}{2}\right) \quad (3.23)$$

In this equation, the argument of the sine term is the quantity which varies to match the applied current, or the DC Josephson Effect component, and the cosine term is the term periodically dependent on the magnetic flux quantum.

Chapter 4

Data Presentation and Analysis

4.1 Resistance vs. Temperature Measurements

The initial measurements taken of BCJ2, the first sample patterned, did not display superconductivity above 77K, indicating loss of oxygen content in its chemical composition. Upon confirming the lack of a superconducting phase in the sample, the sample was removed from its sapphire mount at which time we realized the sample was fractured. Without knowledge of exactly when the fracture occurred, it was impossible to say whether or not the sample had actually lost oxygen and become an insulator, or if it had been broken before measurement.

When we realized we would be unable to produce our desired results using BCJ2, BCJ3 was quickly patterned and all steps were taken during processing to avoid catalyzing the loss of oxygen content. Preliminary measurements of BCJ3 taken in the blue dewar in CNS 211 showed no superconductivity above 77K. To check for superconductivity at a lower transition temperature, BCJ3 was placed in the low temperature lab closed cryogenic cooling system. This cooling system can reach sample temperatures near 20K, allowing for collection of resistance vs. temperature

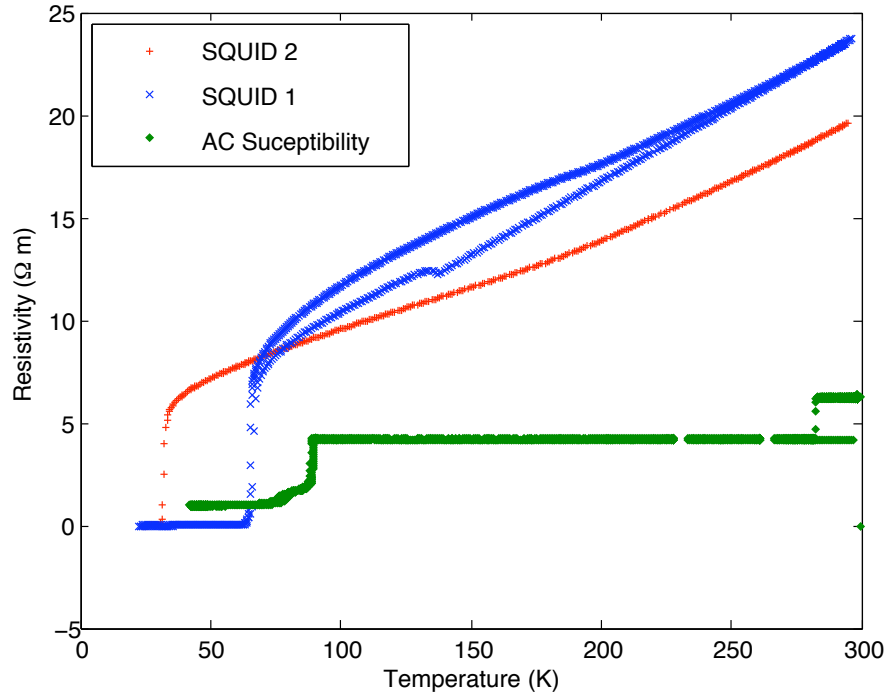


Figure 4.1 Plot of the resistance vs. temperature for each SQUID patterned onto bi-crystal junction sample 3. The hysteresis observed in SQUID 1 is a result of the thermometer temperature lagging behind the real temperature of the sample during cool down. The smoother curve is during the warm up and is more accurate. The AC Susceptibility data is a set of ratios expressed in arbitrary units so no axis labels were used.

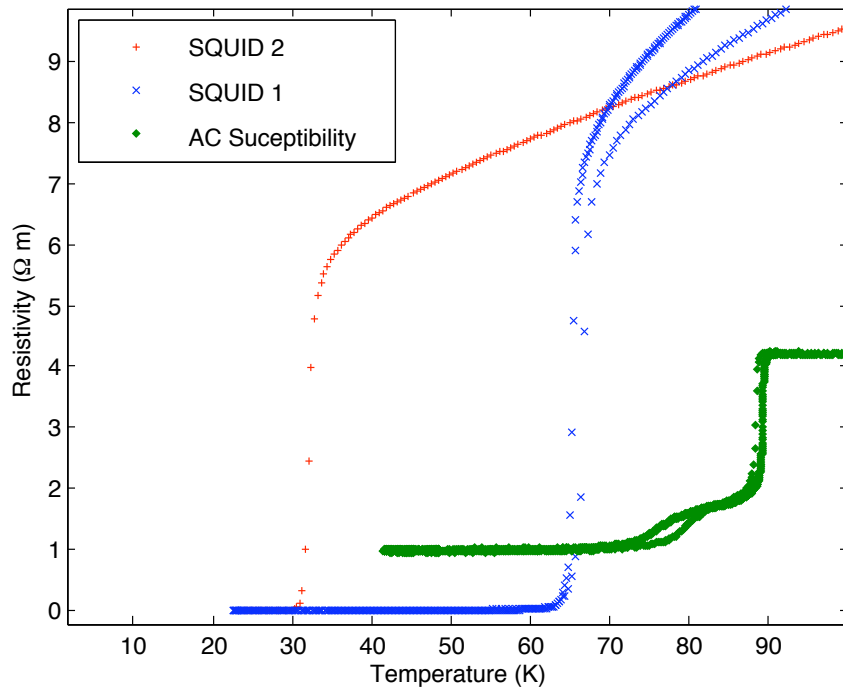


Figure 4.2 Close up of the transition region of each SQUID patterned onto bi-crystal junction sample 3. This close up region shows the drastic shift in transition temperature that occurred during processing. The hysteresis in SQUID 1 is visible again here, and is the result of measuring the sample through cool down and warm up.

data comprehensive enough to determine the resistivity of the sample, whether or not a transition occurs at all and give a best guess of the oxygen content of the sample. Plots of the resistivity vs. temperature for each SQUID on BCJ3 were taken, and are shown in Fig. 4.1. A closer look at the transitions of each SQUID are shown in Fig.4.2. The apparent superconducting phases of each SQUID are seen in this figure to be incomplete. The small and constant but non-zero resistance values persisting after the transition occurs in each SQUID can be attributed to the Josephson Junctions of each SQUID. The small width and length of these sections appears to have accelerated the de-oxidation of their chemical compositions, resulting in no observed superconductivity in the most critical portion of the sample.

After confirming the expected under-doped composition of sample BCJ3, a decision was made to attempt to re-oxidize the sample. The sample was placed in a furnace with an oxygen line running over the sample. The furnace was heated to 200° C at 5° C per minute, remaining at 200° C for two hours. After this re-annealing process the sample was re-wired and resistance vs. temperature curves were again taken for each SQUID. Those curves can be seen in Fig. 4.3. The sharp discontinuities occurring at 230 K and 170 K would usually be considered anomalous behavior associated with poor contacts somewhere down the line, but the fact that it occurs in both samples suggests otherwise. Sadly, otherwise is all that can be said at this point. The behavior is irregular and uncharacteristic of any common superconducting, semiconducting, insulating or metallic material. Moreover, the cryogenic system was used only a day earlier to collect data for Fig. 4.1, and those curves show no irregular behavior which could be attributed to poor contacts.

The only question remaining following the re-annealed measurement was, what does the resistance vs. temperature curve for the unprocessed sample remaining at the CNF look like? If the transition is low, like that of BCJ3 then we can conclude that

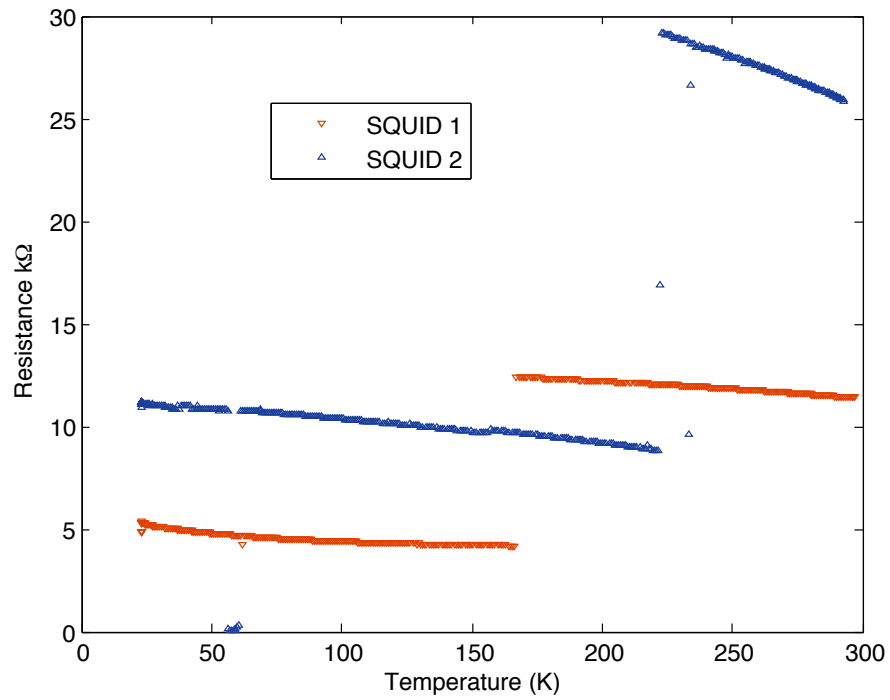


Figure 4.3 Plot of the resistance vs. temperature for each SQUID patterned onto bi-crystal junction sample 3 after the sample was re-annealed. The sharp discontinuities in each SQUID are most likely the result of poor contacts, but all connections were measured before taking this data and showed no such behavior.

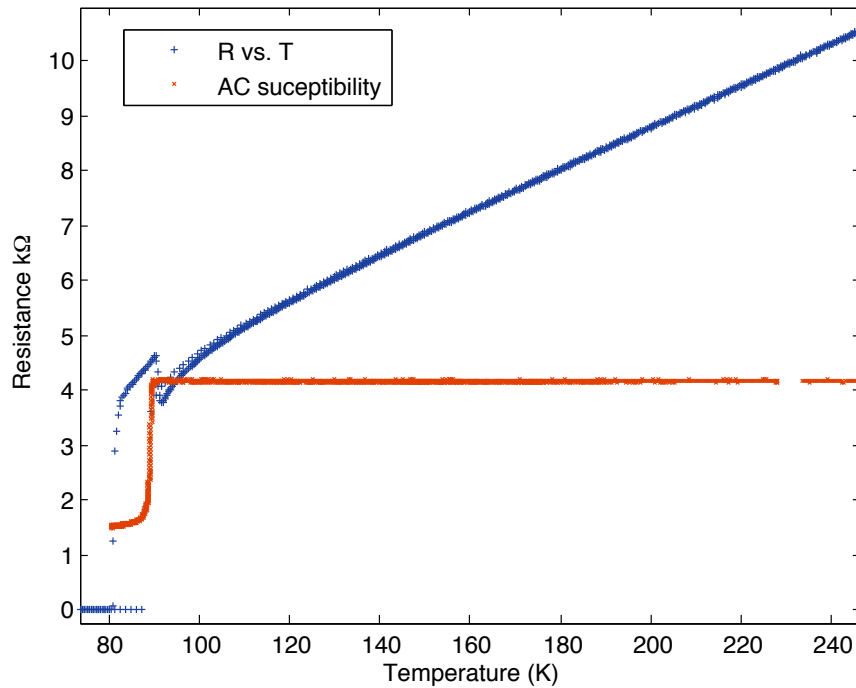


Figure 4.4 Plot of the resistance vs. temperature for un-patterned bi-crystal junction sample 1, the sample accidentally broken in November. Again, AC susceptibility is a ratio so arbitrary units are used and not labeled on an axis. The steep jump in the resistance measurement is most likely poor contacts, and the agreement of the first transition with the original AC susceptibility data suggests some influence external to the sample itself (contacts) are the cause of the discontinuity.

the desiccant intended to maintain the oxygen content in the samples was bad, causing all three samples' transition temperatures to drop dramatically as a result of overexposure to atmosphere. If the transition temperature matches the value measured in July, then we can conclude that some step in the processing of the samples consistently destroyed the superconducting phase. The measurement of BCJ1 was taken from the more damaged of the two pieces BCJ1 resulting from the accident in November. The sample was wired via a simple 4 point measurement, and data collected from this unprocessed sample is shown in Fig. 4.4

The transition temperature of the unprocessed sample, although not as high as it was in July, has not degraded nearly as dramatically as the other two samples. The transition temperature of 80K can be attributed to the age of the sample. All thin film samples of YBCO will de-oxidize over time, even if they are stored in ideal conditions. The fact that the differences observed in these samples is so vast suggests another factor, aside from time, has affected the processed bi-crystal samples.

4.2 Analysis of Data

The loss of oxygen content is apparent in Fig. 4.1. Comparing the observed transition temperatures of the two SQUIDs on sample BCJ3 to figures 4.5 and 4.6 allows for a rough approximation of the oxygen content of each SQUID. SQUID 1 displays a transition temperature of 65K, and SQUID 2 displayed T_c of less than 35K. The transition temperature values can be used to approximate the delta values of each SQUID based on figure 4.5. Amazingly enough, SQUID 1 has a $\delta \approx 0.25$, while SQUID 2 has a $\delta \approx 0.6$. Quite a large discrepancy considering they are separated by less than 2mm on a film that displayed consistent superconductivity in July. However, 4.6 tells a different story. Comparing the calculated resistivity values shown in 4.1

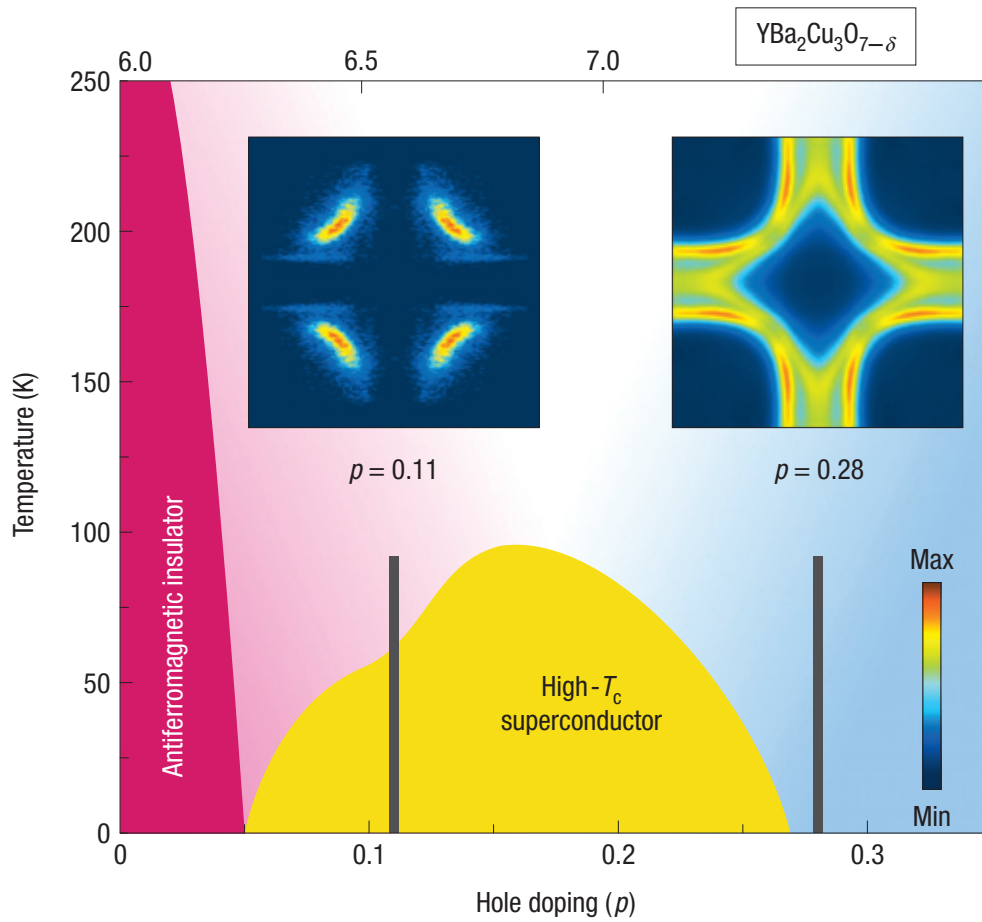


Figure 4.5 Phase diagram of YBCO showing the temperature dependence of the phases vs. oxygen content, figure from Ref. [10]

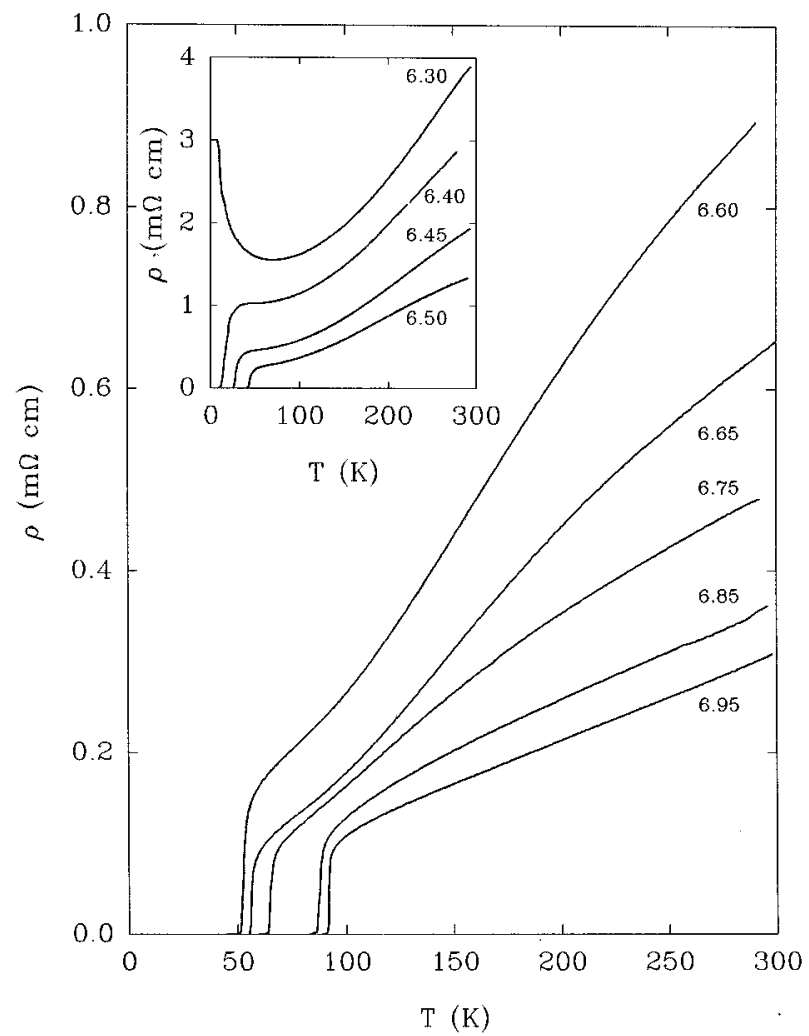


Figure 4.6 Resistivity vs. Temperature for delta values ranging from 0.05 to 0.4, figured borrowed from Ref. [11]

to those displayed in 4.6 suggests that the samples have not lost nearly as much oxygen. According to 4.6, room temperature resistivities around $20\Omega\text{m}$ correspond to $\delta = 0.05$, which is one fifth and one twelfth the phase diagram calculated δ values of SQUID 1 and SQUID 2, respectively.

The large discrepancy between crystal quality of the two SQUIDs on sample BCJ3 and the preserved quality of the superconducting phase in sample BCJ1 all suggest that some aspect of the sample processing is flawed. Without intermediate resistance vs. temperature data, it is impossible to say what exact step causes the oxygen loss. However, it can be said that the exact same processing steps have been executed on other films grown at the same time as the bi-crystals, but with different lithographic masks, and produced correctly patterned, superconducting samples, see ref. [15].

Chapter 5

Conclusion

The mechanism producing the loss of oxygen content in one or both processed samples is at this time still unknown. The measurement of sample BCJ1 has narrowed the field of possible causes down to the steps involved in sample processing. Skipping the evaporation step during the processing of BCJ3 eliminates that step as a potential cause. Left with only this knowledge it is impossible to pin point the cause; However, the only difference between the processing of the samples presented here and others successfully processed by members of our low temperature lab is the lithography mask used. That in mind I would recommend that the next student to attempt this measurement re-think the mask design and make a new one.

Considering the size and scope of this project, although the final measurement was never completed, we have made several advances to that end. All the materials required for growing another bi-crystal sample are paid for and ready to use. The photolithographic masks need to be re-designed, but there are students in the department with enough experience in the CNF to make the new mask and pattern another SQUID sample. The experimental apparatus has been repaired and tested multiple times, and has shown no signs of leaks or thermal sinks. As a part of the project,

nanovoltmeters and current sources were purchased to use with the apparatus and wires as well as conversion boxes were made to accompany them. These materials have also been tested and are in good working order. The only work left to a student that chooses to take up this project is to re-design the mask, pattern the SQUID, and program the data acquisition. That said, I would like to take the remainder of this chapter to pass on advice to any future Ithaca College physicists who so choose to undertake this project.

Starting from the beginning, when growing the samples, uniform heating is of the utmost importance, so take care to smooth any bubbles out of the silver adhesive before adhering the sample to the heater. Following deposition, the annealing of the sample must be taken very seriously, as this phase of PLD produces the desired oxygen content in the sample. Practice on other samples before growing on a bi-crystal substrate, as annealing properly is difficult and can not be reversed or repeated if done incorrectly. When storing the samples, make sure the desiccant is always fresh, and leave a wired sample in the same container as the bi-crystals. This wired sample should be comprehensively measured before it is placed in with the bi-crystals, and measured monthly to ensure the bi-crystals are being safely stored.

When designing masks with Layout Editor, ALWAYS CHECK THE PATTERN BEFORE PROCESSING A MASK. Layout Editor features such as converting layers, adding and subtracting layers, merging objects, grouping and ungrouping cells, and file conversions can all have unintended consequences, and all aspects of a pattern should be checked for correctness regularly during the designing process.

While processing at the CNF, never use primers, they are very hard to clean if the pattern exposure is bad, and do little to better the results if the pattern is good. Also, while using any contact alignment machine, NEVER USE ANY VACUUM. Not to hold the substrate in place, not to hold the substrate chuck to the mask,

not to decrease the spacing between the two. The irregular shape of the rectangular samples produce anisotropic stresses and strains when placed under vacuum, and two rectangular samples were broken in this manner. When milling the sample, take care not to over-mill. Both bi-crystals I milled had milling times considerably lower than other YBCO samples. Overmilling can overheat the sample causing de-oxidation, as well as alter the composition of the substrate and produce undesired conduction. When wiring the sample at IC, do not evaporate gold or chrome onto the sample. Temperatures in the evaporation chamber are far too high for YBCO and may contribute to loss of oxygen content. Immediately upon returning the sample to CNS, cover the middle of the sample in PR to limit the exposure of the critical elements to atmospheric conditions. After measuring the sample in the dewar, if it is to be left in the dewar, fill the dewar with helium to store the sample in non-vacuum and non-atmospheric conditions. If a successful SQUID is processed, an operational amplifier may be necessary to view the oscillatory behavior of the voltage.

Appendix A

Pulsed Laser Deposition

Pulsed Laser Deposition (PLD) is a common technique used to grow crystalline materials under controlled circumstances; it is a standardized and regulated technique but each material is different so critical thermodynamic parameters, order of steps, attention to detail, and other variations associated with the setup of the apparatus are common. The specific PLD methods I used for growing the samples presented in this paper are an adaptation of the methods outlined in my advisors dissertation, [14] and are standard for the Ithaca College Low Temperature Lab. Across all methods of PLD though, the main principal remains the same; superheating a bulk sample of the desired material with a pulsed monochromatic laser to produce a plasma plume directed towards the heated substrate whose specific crystalline structure influences condensation of the plasma plume into the desired crystalline lattice.

A.1 Sample Cleaning

Substrates of SrTiO_3 are cleaned 3 times before deposition, 6 minutes in the sonicator in each of three solvents: Acetone, Methanol, and Isopropanol. After each sonication,

the sample is rinsed with the next solution and dried via a compressed nitrogen line. This process is repeated three times for each substrate before deposition, to ensure the surface of the substrate is clean. Any stray particles remaining on the substrate when it is placed in the chamber for deposition either evaporate off and contaminate the chamber, or could remain on the sample and produce discontinuities in the crystal growth.

A.2 Chamber Cleaning and Sample mounting

Before a deposition can begin, the heater and the bulk material target must be sanded smooth. The interior of the chamber should also be cleaned, and vacuum grease reapplied to all O-ring seals whenever the chamber is opened for an extended period of time. The silver adhesive solution is then applied to the middle of the sample stage, and the substrate is placed face up upon the adhesive. After ten minutes, the heater can be reinserted into the chamber, and pump down can begin.

A.3 Initial pump down and Pre-ablation

Once all necessary elements are prepared and the chamber is sealed, the roughing pump can be turned on. The chamber is then roughed to 5 Torr and the turbo pump can be turned on. The rotor on the turbo pump takes time to reach sufficient speeds for high vacuum. After the rotor surpasses 100 RPM, the turbo pump can be switched to high. The chamber is then pumped down to 10^{-5} Torr. Oxygen gas can then be added to the chamber, up to a pressure of 150 mTorr. The chamber is now ready for pre-ablation, and the laser can be turned on. The laser repetition rate is set to 10 Hz, the sample is covered by a shutter, the bulk material target's rotation is turned

on and the target is pre-ablated for 5 minutes. Pre-ablating the target allows for the laser to remove any impurities from the target which could otherwise land on the substrate. Pre-ablation also heats the target so optimal plasma is produced during deposition.

A.4 Second pump down

After pre-ablation, the laser is turned off, the rotation of the target is turned off, the shutter covering the sample is removed, and the sample stage heater is set to 800° C. As the sample stage heats, the pre-ablation gasses are pumped back out and the chamber must return to a pressure lower than 3×10^{-5} Torr.

A.5 Deposition

For deposition, the laser is turned on and set to 10Hz, the sample rotation is turned on, and oxygen gas is again added to a pressure of 150 mTorr. The rotating target is struck by the laser, creating a plume of $\text{YBa}_2\text{Cu}_3\text{O}_{6.5}$ which is directed at the heated sample. The heated sample acts as a catalyst for the proper alignment of the $\text{YBa}_2\text{Cu}_3\text{O}_{6.5}$ as it slowly forms a crystal atop the SrTiO_3 substrate. The deposition lasts for a total of 15 minutes, after which the laser is shut down and the rotation is turned off.

A.6 Annealing

Immediately after the deposition is complete, oxygen is added to the chamber until it reaches a pressure of 185 Torr. The heater is then shut off and the sample is left to cool down to room temperature in the oxygen rich environment. This step,

known as annealing, forces the extra oxygen atoms this is necessary in order to turn $\text{YBa}_2\text{Cu}_3\text{O}_{6.5}$ into $\text{YBa}_2\text{Cu}_3\text{O}_{7-\delta}$ (into the already heated crystal lattice of the newly grown ceramic). It is this crucial step that produces the desired properties, i.e. zero resistivity below T_C , high T_C , and diamagnetism, in the superconducting sample.

A.7 AC Susceptibility

After the sample has cooled and has been removed from the PLD chamber, an initial measurement is taken to give a rough value of the superconducting phase transition and the width of that transition. The sample is placed in a probe between two wire coils, and an AC current is driven through one of the coils. The entire probe is then placed in a helium dewar and slowly lowered towards the level of the liquid helium. Once the sample becomes superconducting, the magnetic field generated by the driving AC loop is expelled by the sample and the pick up loop shows no induced EMF.

Appendix B

Photolithography

Photolithography is a process of micro and nano fabrication used to transfer computer generated patterns from a chrome plated pane of glass to thin film samples. The process starts by designing the patterns with Computer Aided Design software, and then using a machine to write that pattern onto a chrome plated glass pane, called a photolithography mask, or just a mask. The translation of the pattern is made possible by a class of engineered polymers known as "Photoresists". Photoresists are polymers engineered to react and break down when exposed to specific wavelengths of light, typically in the violet to ultraviolet range. By selectively exposing only portions of the photoresist on the mask, the chrome underlying the desired pattern can be exposed, while leaving the rest of the resist intact. This allows for the removal of the exposed chrome, leaving a translucent desired pattern and a mirror finish everywhere else. Photoresist is then applied to the sample, and the same idea is repeated using the mask to selectively develop the photoresist on the sample. With the desired pattern photoresist intact, the exposed parts of the sample crystal are removed either by ion milling or acid etching.

B.1 Layout Editor

Layout Editor is a Computer Aided Design software specifically designed for photolithography and other nano-fabrication techniques. For this project Layout Editor was used to design three separate types of superconducting elements, the overall pattern of the sample, and a large photolithography mask containing 40 different choices for mask patterns. Of those 40, 34 were unique patterns comprised of different combinations of superconducting elements, and 6 were special mask patterns necessary for certain steps in the photolithography process.

The three separate types of superconducting elements designed in Layout Editor were; SQUIDs, Josephson Junctions, and the standard resistance vs. temperature measurement pattern. Within each of these element types multiple versions were designed with varying dimensions in the section of the sample to be measured. In total, seven unique SQUIDs were designed, four unique Josephson Junctions, and four unique resistance vs. temperature patterns. The variable dimension in the SQUID pattern is the width of the wires as they cross the crystal junction; taking values of two, three, four, five, six, eight and ten microns. The variable dimension in the Josephson Junction is also the width of the wire as it crosses the crystal junction, although only values of two, three, four and six microns were used. The variable dimension in the resistance vs. temperature measurement pattern was the length of the section of wire being measured, with lengths of eighty, one hundred, and one hundred and twenty, all having a width of ten microns; the fourth pattern repeats the one hundred and twenty micron length, but is doubled in the width, for a total of twenty microns.

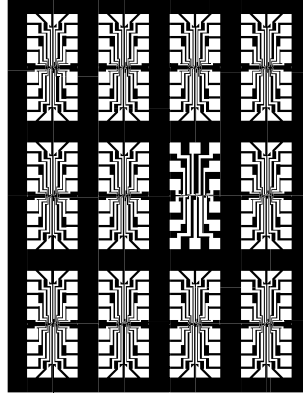


Figure B.1 image from layout editor of the final mask used to pattern the bi-crystal junction thin films into SQUIDs and Josephson Junctions.

B.2 Mask Making

Photolithography masks start out as five inch panes of chrome plated glass, coated in *S1813* photoresist, purchased from the CNF store. Patterns created in CAD are converted into GDSII files, which are converted in to binary data via command line while in the CNF and fed directly into the Mann 3600 Pattern Generator. The PG can produce up to 5000 flashes per hour, with each developing a small rectangle of the entire pattern. Once the entire pattern has been exposed, the mask is removed from the PG and placed in an automatic PR Developer and Chrome Etcher. After Etching, any remaining PR is stripped off with two consecutive baths in a corrosive solution at 75° C and 100° C, respectively. After the baths the mask is compared under microscope with the CAD pattern, and baring any inconsistencies is ready for use.

B.3 Primary Photoresist Spinning

The first step in the photolithographic process for the sample is cleaning. Much like the substrate cleaning during PLD, the sample is placed in a sonicator in an acetone bath for 6 minutes. Afterwards it is repeatedly rinsed with methanol and dried with nitrogen until shiny. Photoresist *S1813* is then applied in a small drop to the center of the sample, while the sample is held by vacuum to the center of a spin station chuck. The spinner is immediately activated, and spun for 60 seconds at 6000 RPMs. The sample is then taken out of the spinner and baked on a 90° C hot plate.

B.4 Primary Photoresist Exposure and Development

The next step in the photolithographic process is the exposure of photoresist on the sample in the desired pattern transferred from the mask. This is done using the ABM contact aligner, but without using the vacuum capabilities of that machine. Early exposures not using BCJ samples were fractured along their diagonal because the vacuum stresses in combination with their irregular shape produced unequal forces at points of contact. Once the sample is aligned as best as possible, the alignment system is deactivated and the exposure timer is set. For the primary pattern exposure, 3.3 seconds of 440 nm light was used. The sample is then removed from the ABM and submerged in AZ Developer 300 MIF for 70 seconds, and then submerged in deionized water for another 70 seconds. After these two baths, all unwanted photoresist should be removed and the desired pattern should remain on the ceramic in photoresist.



Figure B.2 Photolithography pattern used to etch away YBCO and make the BCJ visible.

B.5 Phosphoric Acid Etching

An intermediary step in the photolithography process that is only required when working with a bi-crystal junction sample is phosphoric acid etching. This process is implemented to clear away YBCO from the edges of the sample where the bi-crystal line should be visible on the substrate. This is done by exposing the PR coated sample to the pattern shown below

following the development of this pattern, the sample is placed in a solution of 1 part H_3PO_4 and 100 parts H_2O for 20-25 seconds. After this step the process returns to primary photoresist spinning and continues as a non-bi-crystal junction would.

B.6 Ion Milling

The next step in the photolithographic process is the milling of the sample. The CNF Ion Mill is an Argon Ion Mill made by Veeco. See Fig.B.3 for a visual representation

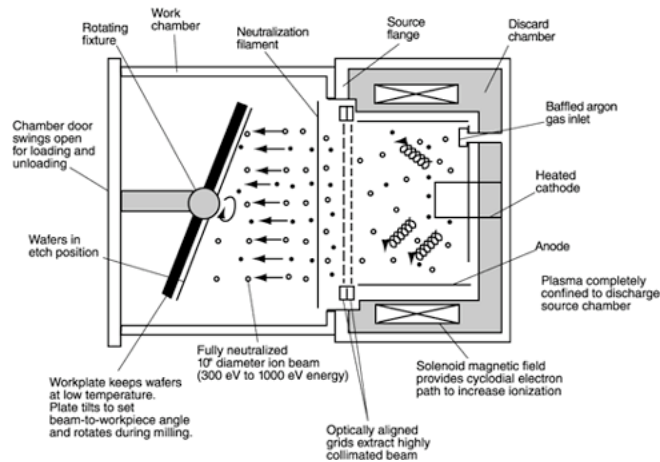


Figure B.3 Simple Diagram showing how the Ion Mill works. <http://www.ionbeammilling.com/images/IonBeamMiller.gif>

of how the machine works. The process from the outside is simple. Insert the sample, pump down to 5×10^{-6} Torr, turn on the power sources and check all the parameters, and start milling. The first 10 minutes of milling follow a pattern of 15 seconds milling, 45 seconds under shutter. After ten minutes the pattern can be switched to 30 seconds on, 30 seconds off. The sample must be periodically checked during the milling process, to ensure the sample is not over or under milled when the machine is turned off. usual milling times from our group for $S1813$ on $YBa_2Cu_3O_{7-\delta}$ are between 45 and 55 minutes total milling.

B.7 Secondary Photoresist Spinning, Exposure and Development

When the sample has been milled sufficiently, a second photoresist pattern can be applied to the sample. this pattern covers the entire surface of the sample in PR, except the contact pads of the sample. The purpose of this pattern is to expose

the contact pads to chrome and gold evaporation, while protecting the rest of the film. Spinning and Development parameters are identical for this step, but over exposure with the ABM is suggested, about 8 seconds, because the contact pads are macroscopic and simple shapes, they can not be effected by overexposure issues, and the extended exposure time ensures the contact pads are clear of PR and ready to stick to chrome.

Appendix C

Layout Editor

Layout Editor is a Computer Aided Design (CAD) program created specifically for designing photolithography masks. Other software exists that serve the same purpose, including L-edit, which is a shareware version of Layout Editor. One of the important aspects of the Layout Editor design scheme is cellular architecture. Users can make as many cells as they please and integrate them together as many times as they please, making yet another cell. To give an example of how this works, I will show explicitly the cellular architecture of my CAD file I used to make my mask. First, an example of the smallest cells from the hierarchy, Fig.C.1, this is a SQUID from the SQUID class of cells, one of the three classes of lowest level cells in the hierarchy. The other two classes are Josephson Junctions, and resistances vs. temperature bridges. Each class of cells on the bottom level of the hierarchy is a group of nearly identical measurement devices, designed with only one or two dimensions changing from one class element to the next. The SQUIDS all share common dimensions in the wire and loops, with the only difference being junction wire width. SQUID wires are all 10 microns, and all the loops are 15 microns wide and 60 microns high. All Josephson Junctions have wire widths of 20 microns, with the junction crossing wire being variable in width

Table 1. Final Photolithography Mask Key

Patterns 1, 5, & 9	Patterns 2, 6, & 10	Patterns 3, 7, & 11	Patterns 4, 8, & 12
2 μm SQUID	3 μm SQUID	4 μm SQUID	5 μm SQUID
2 μm Junction	4 μm Junction	6 μm Junction	2 μm Junction
4 μm Junction	6 μm Junction	8 μm Junction	8 μm Junction
3 μm SQUID	4 μm SQUID	5 μm SQUID	6 μm SQUID
6 μm SQUID	8 μm SQUID*	88 μm R vs. T	2 μm SQUID
2 μm Junction	4 μm Junction	100 μm R vs. T	2 μm Junction
6 μm Junction	8 μm Junction	128 μm R vs. T	198 μm R vs. T
8 μm SQUID*	8 μm SQUID	198 μm R vs. T	4 μm SQUID
3 μm SQUID	4 μm SQUID	5 μm SQUID	6 μm SQUID
4 μm Junction	6 μm Junction	8 μm Junction	4 μm Junction
100 μm R vs. T	88 μm R vs. T	128 μm R vs. T	128 μm R vs. T
5 μm SQUID	6 μm SQUID	8 μm SQUID*	8 μm SQUID

Table 1. *This SQUID differs from the rest in wire width, all wires on this SQUID are 20 microns

and constant in height, 10 microns. All the R vs. T elements have wire widths of 20 microns, and resistor widths of 10 microns. A table giving the dimensions, both dynamic and constant, of each type of measurement element is given below.

Going up one level from the measuring elements, the sample pattern level of cell classes are second in the hierarchy. At this level there were originally 7 classes,

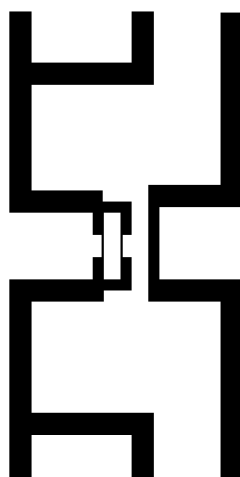


Figure C.1 Layout Editor schematic of a SQUID element. The common wire width on this element is 10 microns, the width of the loop is 15 microns, the height of the loop is 60 microns, and the width of wire crossing the junction varies from SQUID to SQUID.

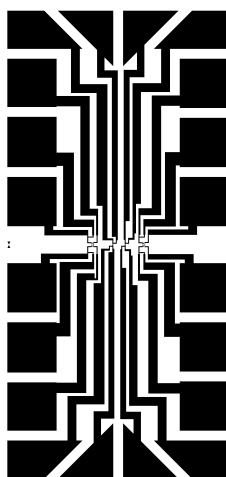


Figure C.2 4 Element photolithography pattern used to expose a 4 element pattern onto a layer of photoresist on a $5mm \times 10mm$ thin film.

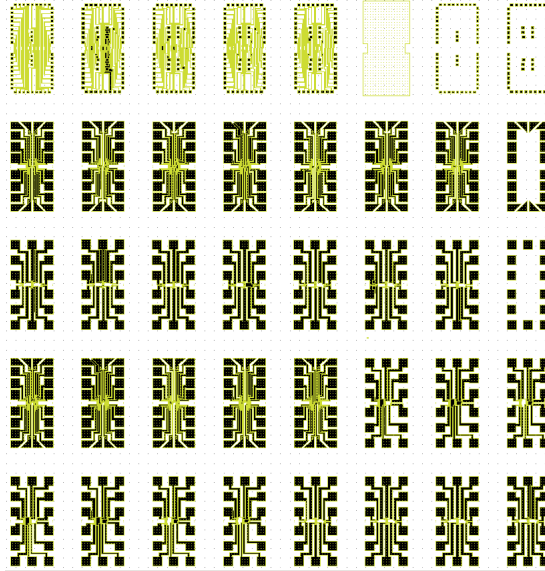


Figure C.3 Image of Layout Editor file used to pattern my first 5×5 inch photolithography mask. each element on the mask is designed for patterning onto a $5mm \times 10mm$ thin film.

All other cell classes designed during the CAD process are listed and shown here.

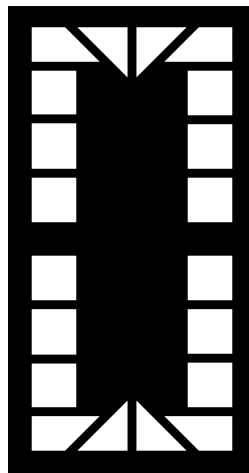


Figure C.4 photolithography pattern used for exposing only the contacts of a 4 element $5mm \times 10mm$ thin film pattern.

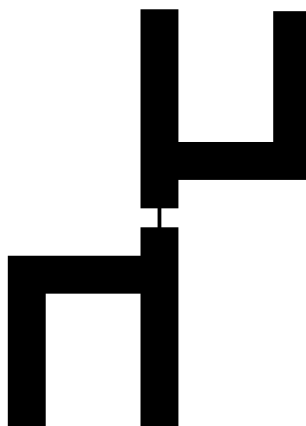


Figure C.5 Layout Editor schematic of a Josephson Junction element. The common wire width on the Josephson junction elements is 20 microns, and the height of the wire crossing the junction is always 10 microns.

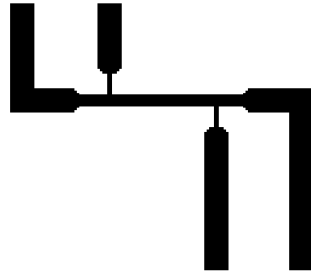


Figure C.6 Layout Editor schematic of an R vs. T measurement element. The common wire width for R vs. T elements is 20 microns, and the height of the measured portion of wire is always 10 microns.

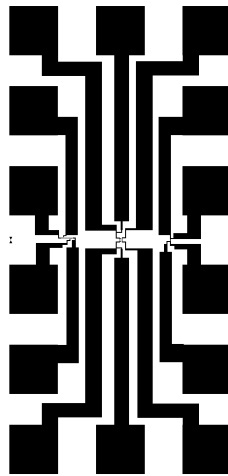


Figure C.7 3 Element photolithography pattern used to expose a 3 element pattern onto a layer of photoresist on a $5mm \times 10mm$ thin film.

Appendix D

Experimental Apparatus Photos



Figure D.1 Picture of the top of the Dewar / Vacuum Chamber used in CNS 211 for all measurements.



Figure D.2 Picture of the bottom of the Dewar / Vacuum Chamber used in CNS 211 for all measurements.

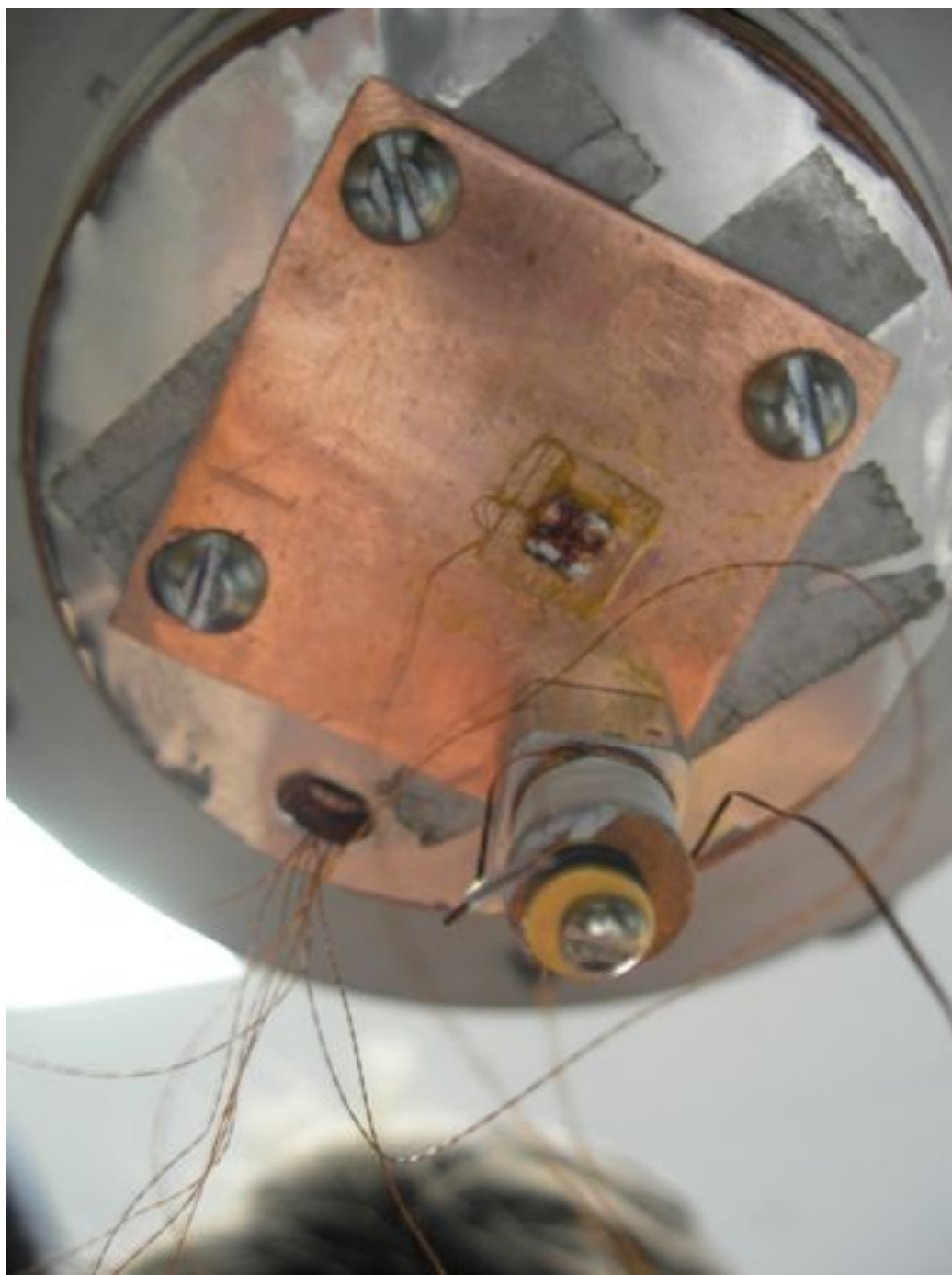


Figure D.3 Picture of the sample stage at the bottom of the cold head inside the dewar in CNS 211.

Bibliography

- [1] M. Tinkham, *Introduction to Superconductivity*, 2nd ed. (Dover, New York, 2004)
- [2] J. R. Hook and H. E. Hall, *Solid State Physics*, 2nd ed. (Wiley & Sons, Chichester, 1991)
- [3] B. D. Josephson, “Possible New Effects In Superconducting Tunnelling,” *Physics Letters* **1 no. 7**, 251 - 253 (1962).
- [4] R. C. Jaklevic, J. Lambe, J. E. Mercereau and A. H. Silver, “Quantum Interference Effects in Josephson Tunneling,” *Phys. Rev. Lett.* **12, no. 7** 159 – 160 (1964).
- [5] R. C. Jaklevic, J. Lambe, J. E. Mercereau and A. H. Silver, “Macroscopic Quantum Interference in Superconductors,” *Phys. Rev.* **140, no. 5A** 1628–1637 (1965).
- [6] P. W. Anderson and J. M. Rowell, “Probable Observation Of the Josephson Superconducting Tunneling Effect,” *Phys. Rev. Lett.* **10, no. 6** 230–232 (1963).
- [7] R. H. Koch, C. P. Umbach, G. J. Clark, P. Chaudhari, R. B. Laibowitz, “Quantum Interference Devices made from Superconducting Oxide Thin Films,” *Appl. Phys. Lett.* **51, no. 3** 315–318 (1987).

- [8] R. Gross, P. Chaudhari, M. Kawasaki, M. Ketchen and A. Gupta, "Noise Characteristics of single grain boundary junction DC SQUID's in $\text{YBa}_2\text{Cu}_3\text{O}_{7-\delta}$ films," *Physica C* **170**, no. 2 315–318 (1990).
- [9] J. G. Bednorz and K. A. Müller, "Possible high T_c superconductivity in the Ba-La-Cu-O system", *Z. Physik*, **vol. 64**, 1986 p. 189–193
- [10] M. A. Hossain, J. D. F. Mottershead, D. Fournier, A. Bostwick, J. L. McChesney, E. Rotenberg, R. Liang, W. N. Hardy, G. A. Sawatzky, I. S. Elfimov, D. A. Bonn, and A. Damascelli, "In situ doping control of the surface of high-temperature superconductors", *Nat Phys*, **vol. 4 issue 7**, p. 527–531, 2008
- [11] B. Wuyts, V. A. Moschalkov, and Y. Bruynseraede, "Resistivity and Hall effect of metallic oxygen-deficient $\text{YBa}_2\text{Cu}_3\text{O}_x$ films," *Phys. Rev. B* **53**, no. 14 9418–9432 (1996).
- [12] W. J. Bencze, S. Buchman, B. Clarke, D. DeBra, C. W.F. Everitt, G. Green, M. I. Heifetz, D. N. Hipkins, G. M. Keiser, J. Li, J. A. Lipa, B. Muhlfelder, B. W. Parkinson, A. S. Silbergleit, M. Taber, J. P. Turneaure, S. Wang, "Gravity Probe B - Testing Einstein at the Limits of Engineering," *Nuclear Physics B - Proceedings Supplements* **166** 147 - 152 (2007)
- [13] S. Y. Lee, "Multi-channel Scanning SQUID Microscopy," College Park M.D. : University of Maryland, 2004.
- [14] M. C. Sullivan, "The Normal-Superconducting Phase Transition of YBCO in Zero Magnetic Field," College Park M.D. : University of Maryland, 2004.
- [15] C. P. Strehlow, "Measuring the Superconductivity Phase Transition in YBCO," Ithaca, N.Y. : Ithaca College, 2008.